ACS APPLIED MATERIALS & INTERFACES

www.acsami.org

Research Article

Phosphate-Driven Interfacial Self-Assembly of Silk Fibroin for Continuous Noncovalent Growth of Nanothin Defect-Free Coatings

Caleb Wigham,[+] Tanner D. Fink,[+] Mirco Sorci, Padraic O'Reilly, Sung Park, Jeongae Kim, Vrushali R. Varude, and R. Helen Zha*

Cite This: *ACS Appl. Mater. Interfaces* 2024, 16, 58121−58134

Read Online

ACCESS | Metrics & More | Article Recommendations | Supporting Information

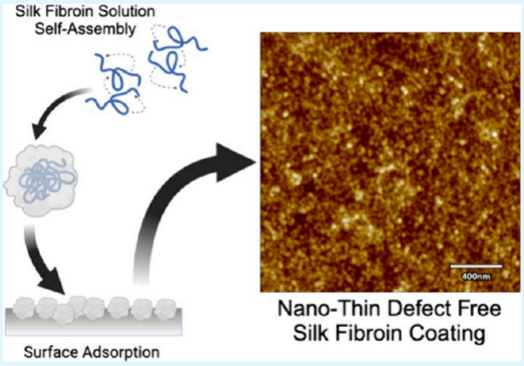

ABSTRACT: Silk fibroin is a fiber-forming protein derived from the thread of *Bombyx mori* silkworm cocoons. This biocompatible protein, under the kosmotropic influence of potassium phosphate, can undergo supramolecular self-assembly driven by a random coil to β-sheet secondary structure transition. By leveraging concurrent nonspecific adsorption and self-assembly of silk fibroin, we demonstrate an interfacial phenomenon that yields adherent, defect-free nanothin protein coatings that grow continuously in time, without observable saturation in mass deposition. This noncovalent growth of silk fibroin coatings is a departure from traditionally studied protein adsorption phenomena, which generally yield adsorbed layers that saturate in mass with time and often do not completely cover the surface. Here, we explore the fundamental mechanisms of coating growth by examining the effects of coating solution parameters that promote or inhibit silk fibroin self-assembly. Results show a strong dependence of coating kinetics and structure on solution pH, salt species, and salt concentration. Moreover, coating growth was observed to occur in two stages: an early stage driven by protein−surface interactions and a late stage driven by protein−protein interactions. To describe this phenomenon, we developed a kinetic adsorption model with Langmuir-like behavior at early times and a constant steady-state growth rate at later times. Structural analysis by FTIR and photoinduced force microscopy show that small β-sheet-rich structures serve as anchoring sites for absorbing protein nanoaggregates, which is critical for coating formation. Additionally, β-sheets are preferentially located at the interface between protein nanoaggregates in the coating, suggesting their role in forming stable, robust coatings.

KEYWORDS: *silk fibroin, self-assembly, protein adsorption, noncovalent interactions, biomaterials*

■ INTRODUCTION

Protein adsorption is a "common but very complicated phenomenon" hallmarked by its ubiquity.[1] Most researchers aim to prevent protein adsorption, as it is detrimental to the function of devices, such as biosensors and membranes, and can promote harmful pathologies, such as antibiotic-resistant infections. However, this persistent and promiscuous interfacial phenomenon can also be harnessed as a facile method for increasing the functionality of surfaces, particularly for biomedical applications. For example, adsorption of extracellular matrix proteins, such as collagen[2] and laminin,[3] is commonly used to enhance cellular adhesion and migration, while adsorption of lysozyme[4] and lysostaphin[5] can be used to provide antimicrobial properties. Adsorbed proteins can also serve as initiator points for further surface modifications via "grafting from" polymerization.[6,7] However, the use of protein adsorption as a strategy for surface modification in real-world applications is limited by low surface coverage and desorption in operating environments.

Traditional protein adsorption is usually characterized by a rapid initial adsorption, followed by saturation in mass deposition at the "jamming limit" of the protein,[8−10] which is often due to electrostatic repulsion between adsorbed proteins. Surface coverage due to protein adsorption is typically incomplete (e.g., ∼ 55% predicted by the random sequential adsorption model).[10] The lack of cohesive interactions between adsorbed proteins can also promote easy desorption for proteins that have weak interactions with the substrate. Conditions that facilitate attractive interactions between proteins can be leveraged to allow for "continuous" adsorption at a solid−liquid interface past a typical saturation.[11] For example, bovine serum albumin has been shown to form multilayer coatings at near crystallization conditions in concentrated ammonium sulfate solution.[12] However, upon removal of the ammonium sulfate, repulsive

Received: May 7, 2024
Revised: July 29, 2024
Accepted: October 4, 2024
Published: October 16, 2024

protein−protein interactions caused the coatings to revert to single monolayer thickness.

In contrast, self-assembling proteins can exhibit atypical adsorption behavior. Such proteins can have favorable cohesive interactions through van der Waals, hydrophobic, electrostatic, and hydrogen bonding interactions, which act as noncovalent cross-links.[13−15] Our previous work has shown that self-assembling silk fibroins are versatile bottom-up platforms for modifying biomedically relevant surfaces without requiring reactive surface chemistries or specific adhesion motifs.[16−18] In this noncovalent surface modification strategy, potassium phosphate in a mild aqueous buffer is used to trigger silk fibroin assembly at a solid−liquid interface, generating a dense and well-adhered nanothin coating that grows monotonically in time without saturation. This "universal" coating can form on a wide range of substrates (e.g., hydrophobic, hydrophilic, polymeric, inorganic) without needing surface activation (e.g., via high energy radiation or plasma treatment) for robust adhesion. Moreover, no additional fixation steps are required, as the coating does not desorb or dissolve when the phosphate anion is removed. Our previous work has shown that coating self-assembly can occur with *Bombyx mori*-derived silk fibroin as well as with recombinant proteins that mimic ADF4 dragline spidroin, despite their differences in primary sequence and size.[16−18] These self-assembled coatings can exhibit desirable bioactivity, such as increasing nerve cell attachment and neurite extension,[16] eluting protein payloads from surfaces,[17] and decreasing surface colonization by bacteria.[18]

Phosphate-induced continuous growth of silk fibroin coatings exemplifies an interfacial phenomenon in which adsorption is concurrent with self-assembly, which is poorly described in literature despite likely being common in nature. This one-pot coating process is also distinct from other bottom-up silk coating strategies. Exposure to certain environmental factors, such as solution acidification,[19,20] the presence of phosphate ions,[21] and exposure to alcohols[22] trigger silk fibroin to transform from a soluble protein into an insoluble β-sheet rich material. Wang et al. leveraged this behavior to form multilayer *B. mori* silk fibroin coatings though a stepwise layer-by-layer approach, where silk fibroin was adsorbed onto a surface until saturation and treatment with methanol was then used to fix the adsorbed layer before adding the subsequent layer.[23] Nilebäck et al. demonstrated that the recombinant spidroin 4RepCT was capable of growing well adhered, fibrillar coatings without saturation at a solid−liquid interface.[24] However, complete coverage of the underlying substrate was not demonstrated, and no solution-phase additives (e.g., phosphate) were used to control coating kinetics. We utilize phosphate as the stimulus for silk fibroin self-assembly in our work because phosphate, a kosmotropic anion, is known to promote inter- and intraprotein interactions. Phosphate plays a critical role in the self-assembly of natural spidroins, where it promotes liquid−liquid phase separation[25] and β-sheet formation during spider silk spinning.[26−28] Phosphate has also been previously used to promote β-sheet formation within recombinant spidroin materials[29,30] and *B. mori* silk fibroin particles.[21]

Herein, we seek to elucidate the fundamental mechanisms underlying continuous coating growth by silk fibroin self-assembly. We study the evolution of coating nanostructure and protein conformation during coating formation as a function of solution composition. We complement these studies with investigations of solution-phase self-assembly behavior, which highlights an optimal phosphate concentration for mediating well-controlled growth of smooth, defect-free coatings. We find that silk fibroin coating formation relies on a balance of protein−surface interactions, which dominate in the early stage of coating assembly, and protein−protein interactions, which dominate in the late stage of coating assembly. As existing protein fouling models do not capture this two-stage continuous growth phenomenon, we introduce a novel kinetic model of coating formation. Finally, we demonstrate the potential of self-assembled silk fibroin coatings to serve as versatile noncovalent surface modification for creating non-fouling surfaces.

■ MATERIALS AND METHODS

General Substrate Cleaning Procedure. Silica wafers coated with 100 nm of TiO_2 (University Wafer, Boston, MA) were cleaned by sonicating samples in 10% Simple Green Original Degreaser, ultrapure water, isopropanol, acetone, and ultrapure water for 15 min each, and then dried with air. Immediately prior to coating samples were exposed to UV-ozone (Osilla, Sheffield, UK) for 10 min as a final cleaning step.

General Coating Procedure. Commercially purchased stock solutions of degummed silk fibroin (silk fibroin) derived from the cocoons of *B. mori* (MW ∼ 100 kDa) (Advanced BioMatrix, Carlsbad, CA) were centrifuged at 8400 rcf for 30 min at 4 °C to remove protein aggregates prior to use. Protein concentration was measured at 280 nm using a NanoDrop One Spectrometer (ThermoFisher, MA, USA) with the assumption that 1 abs = 1 mg/mL due to the polydispersity of the silk fibroin molecular weight from the degumming process.[31] Coating solutions were prepared by diluting the silk fibroin to 0.5 mg/mL in ultrapure water with a set volume of a 1.25 M potassium phosphate (KH_2PO_4/K_2HPO_4) stock solution to obtain the desired phosphate concentration. A phosphate concentration range of 100 mM − 500 mM was chosen due to limitations in the buffering capacity below 100 mM, and the tendency of silk fibroin proteins to form precipitated particles above 500 mM.[21] Solution pH was controlled by varying the ratio of monobasic and dibasic potassium phosphate in the stock solution (monobasic, KH_2PO_4, solution pH = 4.0 and dibasic, K_2HPO_4, solution pH = 9.0). Cleaned substrates were immersed in freshly prepared coating solutions in Petri dishes, which were sealed with parafilm to mitigate evaporation, and placed on a shaker with gentle agitation (60 rpm) at room temperature (25 °C). Substrates were coated for the allotted amount of time, removed from the coating solution, washed with excess ultrapure water for 5 min under gentle agitation (60 rpm), and dried with air. Care was taken to ensure that coated substrate did not dry out prior to washing.

Ellipsometry Measurements. Dry coating thicknesses of nanothin silk fibroin coatings on TiO_2 wafers were measured via ellipsometry using a M-44 ellipsometer (J. A. Woollam NE, USA). Spectra between 400−750 nm were obtained at 55°, 65°, and 75° and data was analyzed using the CompleteEase software (J. A. Woollam NE, USA) using a multilayer model consisting of a silicon substrate, a graded TiO_2 Cauchy layer, and a silk fibroin Cauchy layer using optical constants determined from Bucciarelli et al. for silk fibroin films derived from aqueous solutions.[32] For each sample the thickness of the TiO_2 and silk fibroin layers were fit, and typical fits resulted in a mean squared error less than 10. Three biological replicates ($n = 3$) were measured per coating condition. For QCM-D/ellipsometer experiments, only 65° was used for ellipsometry data collection due to flow module design.

Fourier-Transform Infrared Spectroscopy (FTIR). Silk fibroin coating secondary structure content was estimated using FITR. Data accusation was performed using a Vertex 70 Spectrometer (Bruker MA, USA) equipped with a Bruker Platinum attenuated total reflection diamond crystal cell. Absorbance measurements between wavenumbers 600−4000 cm^{-1} were performed with 100 scans and resolution of 4 cm^{-1}. Secondary structure content was determined through multipeak fitting of the amide I region (1595 cm^{-1} − 1700 cm^{-1}) using Igor Pro 8 (WaveMetrics Inc. OR, USA). Peak numbers and positions for deconvolution were determined though second derivative analysis of FTIR spectra, with peak assignments based on Hu et al.[33] Briefly, adsorption bands within the frequency range of 1616−1637 cm^{-1} and 1695−1705 cm^{-1} were attributed to enriched β-sheet structures while bands in the frequency range of 1638−1655 cm^{-1} were attributed to random coil, 1656−1663 cm^{-1} were attributed to α-helices, and 1663−1695 cm^{-1} were attributed to β-turns. Three biological replicates per condition were measured (n = 3).

Dry State Atomic Force Microscopy. Height images of dry nanothin silk fibroin coatings on TiO_2 wafers were obtained using an MFP-3D AFM (Asylum CA, USA) operated in tapping mode with aluminum reflex coated SSS-NCHR cantilevers (NANOSENSORSÔ Neuchâtel, Switzerland) with <2 nm tip radius, 330 kHz frequency, and force constant of 42 N/m. Images were collected at 1024 × 1024-pixel resolution with a scanning rate around 1 Hz. FIJI (National Institute of Health MD, USA) was used for determining average globular size using the straight-line analysis tool, measuring across and through the center of 100 individual globules per sample (n = 100). Asylum Research 16.14.216 software (Asylum CA, USA) was used for determining silk fibroin globule volumes and surface area using the particle analysis feature (n = 100) and for generating height distribution of the AFM images. Deconvolution of the histogram height distributions for estimating surface coverage was done via peak deconvolution using Igor Pro 8 (WaveMetrics OR, USA) (n = 5) using two peaks, with one assigned to bare TiO_2 and another assigned to silk fibroin nanoaggregates.

Hydrated State Atomic Force Microscopy. Height images of nanothin silk fibroin coatings in the hydrated state on TiO_2 wafers were obtained using a Cypher VRS AFM (Asylum CA, USA) at The Center for Functional Materials at Brookhaven National Lab. Samples were imaged in ultrapure water using AC40 BioLever Mini cantilevers (Bruker MA, USA) with 25 kHz frequency in liquid, 0.1 N/m spring constants, and 8 nm tip radius. Images were obtained at 512 × 512-pixel resolution with scanning rates around 1 Hz. Asylum Research 16.14.216 software (Asylum CA, USA) was used for determining average subglobule diameters and heights by drawing a line across and through the centers of the subglobule structures and obtaining the height profiles (n = 5).

Infrared Photo-Induced Force Microscopy (PiFM). Spatial locations of various secondary structures in the silk fibroin coatings were characterized using a noncontact dynamic mode AFM technique known as PiFM performed by Molecular Vista Inc. (San Jose CA, USA). Measurements were performed using a Vista One microscope (Molecular Vista Inc. CA, USA) coupled with a Block Engineering LaserTune quantum cascade laser (QCL), with a range of 1860−772 cm^{-1} and a spectral line width of 2 cm^{-1}. The laser beam was focused via a parabolic mirror on the interface between the sample and metal-coated AFM tip, resulting in an elliptical spot size of approximately $\lambda \times 1.5\lambda$ and average laser power on the sample surface of 100 μW. The laser was modulated at a frequency, f_m, so that $f_m = f_1 - f_0$, where f_0 and f_1 are the cantilever's first and second mechanical resonance modes respectively; this sideband mode uses the quality factor of the cantilever to improve sensitivity. Platinum−iridium-coated NCH 300 kHz noncontact cantilevers (NANOSENSORSÔ Neuchâtel, Switzerland) were used for all measurements. All PiFM and topography images were collected at 256 × 256-pixel resolution and a scan speed of 0.5 to 1 Hz. All data processing was conducted using SurfaceWorks software (Molecular Vista Inc. CA, USA).

Atomic Force Microscopy Force Measurements. Force measurements were conducted using an MFP-3D AFM (Asylum CA, USA) using a custom silk fibroin coated silica probe. Briefly, a 1 μm silica particle (Superior Silica, LLC AZ, USA) was coated in the standard coating solution (200 mM KH_2PO_4/KH_2PO_4, pH 5.0) for 30 min, and affixed to a silicon nitride cantilever (Novascan, IA USA) with force constant of 0.06 N/m. Force measurements between the silk fibroin coated particle and a 3 h silk fibroin coated TiO_2 wafer were conducted in buffers with different solution pH (5.0, 6.5, and 8.0) and phosphate concentration (100 mM, 200 mM, and 500 mM) to understand protein−protein interactions under these conditions. Additionally, the same solution conditions were used to investigate the effects of solution conditions on protein−surface interactions using the silk fibroin coated silica particle and a bare TiO_2 wafer. Force measurements were conducted in force-volume (FV) mode[34,35] across a 1 μm × 1 μm sample surface using a total measured area of 20 μm^2 (n = 400) with a scanning speed of 2 μm/s and a trigger force of 250 pN. AFM cantilevers were calibrated before each experiment using a previously described three-step procedure.[36] Adhesion forces were calculated by analyzing the retraction curves for each force−distance plot using IgorPro 6 (WaveMetrics OR, USA).

Quartz Crystal Microbalance (QCM-D). Coating formation was evaluated using a Biolin Scientific Q-Sense E-4 series quartz crystal microbalance with dissipation monitoring (QCM-D). Coatings were measured on TiO_2 coated AT-cut crystal sensors (QSX 310) and cleaned according to manufacturer specifications. Coating experiments were conducted at 25 °C and a flow rate of 250 μL/min (Re ∼ 1); all solutions were degassed prior to experiment to prevent bubble formation in flow modules. Figure S1 shows maximum protein flux to the QCM-D sensor surface at various flow rates, showing that adsorption rates increase with flow rate until ∼200 μL/min, at which point they plateau (when no phosphate ions are added) or slightly decrease (when phosphate ions are present to promote self-assembly). These results suggest that at least 200 μL/min is required to be in a regime of diffusion-limited transport. Thus, we used a volumetric flow rate of 250 μL/min for our QCM-D studies. Data was collected with QSoft 401 software and imported into QSense Dfind for viscoelastic modeling.[37] All coating kinetic curves presented were extracted from the viscoelastic modeling package while dissipation and frequency plots were from the raw data.

Dynamic Light Scattering (DLS). Protein aggregate diameters were measured using an Anton Paar Litesizer 500 Particle Analyzer. All buffers without protein were filtered using 0.2 μm poly(ether sulfone) (PES) syringe filters prior to measurement to reduce dust contaminants. Solutions were allowed to equilibrate for 2 min prior to measurement to ensure thermal equilibrium; all aggregate studies were completed at 25 °C. Experimental parameters such as number of scans, filtering, and focus were automatically determined by the software for individual samples to increase quality of signal. Scattering angle of 90° was used for all samples. Reported results are volume-weighted averages (n = 4) as reported from the Kalliope software (2.18.0).

Contact Angle Measurements. Surface wettability of silk fibroin-coated and uncoated substrates was assessed using static water contact angle measurements with a DS100 Drop Shape Analyzer (KRÜSS NC, USA). Three microliters of ultrapure water was deposited on the substrate surface, and the angle at the solid−liquid and liquid−vapor interface was fit using the Drop Shape Analysis 4 software (KRÜSS Hamburg, Germany). The left and right-side angles were averaged for each droplet with a minimum of 3 technical measurements per sample, with 3 biological replicates per material (n = 3). Substrates were cleaned according to the general substrate cleaning procedure, but organic substrates were cleaned without exposure to acetone.

Nonfouling Surface Experiments. Nonfouling experiments performed in the QCM-D were conducted with identical parameters described in the preceding section. Silk fibroin and BSA solutions consisted of 200 mM phosphate, pH 5, and 0.5 mg/mL protein to fit within the bounds of instrument limitations. Nonfouling experiment using silica resin (Davisil grade 923) were performed as follows. Five wt % stock of silica resin were coated in 2 mL of the standard silk fibroin coating solution (0.5 mg/mL silk fibroin, 200 mM phosphate, pH 5.0) for 30 min under slow inversion. Samples were purified though centrifugation and were washed with 5x excess ultrapure water to remove any loosely bound silk fibroin. For the BSA fouling studies, silk fibroin coated samples and bare silica particles were incubated in 1 mL of 1x PBS containing 10 mg/mL BSA (1% FITC-BSA) overnight. Adsorbed samples were then rinsed with 5x excess ultrapure water and imaged using a Revolve Fluorescent Microscope

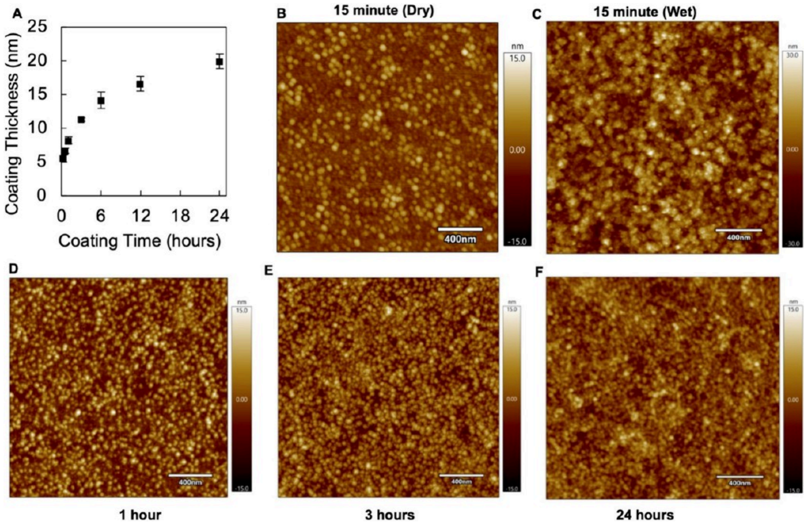

Figure 1. Silk fibroin coating thickness and surface structure at various time points in the coating process. (A) Coating thickness of nanothin silk fibroin coatings measured by spectroscopic ellipsometry. (B−F) AFM images of silk fibroin coating surface structure at various time points in the coating process. Liquid-mode AFM (C) reveals subglobular structures not observed in the dry state images.

(Discover Echo Inc., CA USA) using the FITC filters and 400 ms exposure time.

RESULTS AND DISCUSSION

Silk Fibroin Continuously Self-Assembles into Nanoglobular Coatings in the Presence of Potassium Phosphate. Snapshots of coating formation over time were generated by immersing a TiO_2 substrate, chosen for its common use in medical implants, in an aqueous solution containing dilute silk fibroin (0.5 mg/mL) and potassium phosphate (200 mM, pH 5.0). Agitation on an orbital shaker was used to ensure solution homogeneity during coating formation and to prevent settling of any large aggregates onto the coating surface. However, agitation was kept mild (60 rpm) to prevent large-scale silk fibroin aggregation in solution, as shear forces are known to promote silk fibroin self-assembly.[38] Figure 1A shows monotonically increasing coating thickness, reaching ∼20 nm (dry), over the 24 h observation period. Dry height profile AFM images at discrete time points in the coating process (Figure 1B) show that coatings are comprised of globular aggregates which continuously accumulate on the substrate surface over time. Individual globules at early time points (i.e., 15 min) exhibit slightly larger apparent diameters of 60 ± 7 nm compared to 50 ± 7 nm for multilayer coatings made for 24 h likely due to spreading of the globule structures on the substrate surface. Globular size evolution over 24 h coating growth is provided in Figure S2.

The relatively narrow size distribution of globular aggregates is surprising considering the polydispersity of the fibroin molecular weight due to the degumming process[39] and the natural tendency of silk proteins to assemble into fibrillar structures through a nucleation and growth mechanism.[18,21,31,40−45] At early coating time points (15 min −1 h), portions of the underlying TiO_2 surface are visible while silk fibroin nanoglobules appear to be randomly distributed across the surface. Analysis of AFM images yields surface coverage of 30 ± 5%, 47 ± 4%, and 63 ± 3% for coatings made for 15 min, 30 min, and 1 h, respectively. After 3 h, the underlying substrate becomes no longer observable as globule density increases past full surface coverage. As growth continues, the coating surface remains smooth, globular, and uniform while thickness increases. At long coating time points (i.e., 24 h) the coatings exhibit extremely smooth surfaces, with calculated surface roughness of ∼2.8 nm indicating that the continuous deposition of the silk fibroin globules occurs homogeneously over the substrate surface. This result suggests that under these solution conditions the interfacial self-assembly process is well-controlled, without autocatalytic formation of precipitates or large mounds. The high surface density of silk fibroin is atypical for protein adsorption, which are generally do not reach full coverage (e.g., random sequential adsorption model predicts saturation at ∼55% surface coverage).[10] The ability of silk fibroin to form strong supramolecular interactions in the coating buffer is likely responsible for its high packing density.

Our AFM images suggest that our coatings form though accumulation of globular nanoaggregates onto the surface, rather than nanofibrils previously observed with recombinant spidroins, such as eADF4(C16)[18] and 4Rep-CT.[24] However, it should be noted that nanofibers were observed via AFM when we attempted to form coatings at elevated temperatures (37 °C) to try to enhance the rate of coating formation (data not shown). This is likely due to the influence of elevated temperature on silk fibroin self-assembly, as previously demonstrated by other groups.[46] Analysis of isolated nanoglobules at the 15 min time point allows for an estimation of the number of silk fibroin chains comprising each globule. Analyzing 100 individual nanoglobules using the Asylum AFM software, we calculate their average volume to be $1.31 \times 10^4 \pm 5.35 \times 10^3$ nm^3. Based on an average degummed silk fibroin molecular weight of 100 kDa and a protein density of 1.0−1.3 g/cm^3 in the dry state[47] each nanoglobule is estimated to be comprised of 80−100 individual silk fibroin chains. The silk fibroin coatings swell when imaged in ultrapure water (Figure 1C), suggesting that these coatings are hydrogel-like, which is consistent with previous reports of silk fibroin-based materials.[48] In the hydrated state, nanoglobules can be observed to be comprised of smaller subglobules, which supports their hierarchically assembled nature. It is difficult to estimate the number of silk fibroin molecules present in these subglobules due to the difficulty of isolating individual

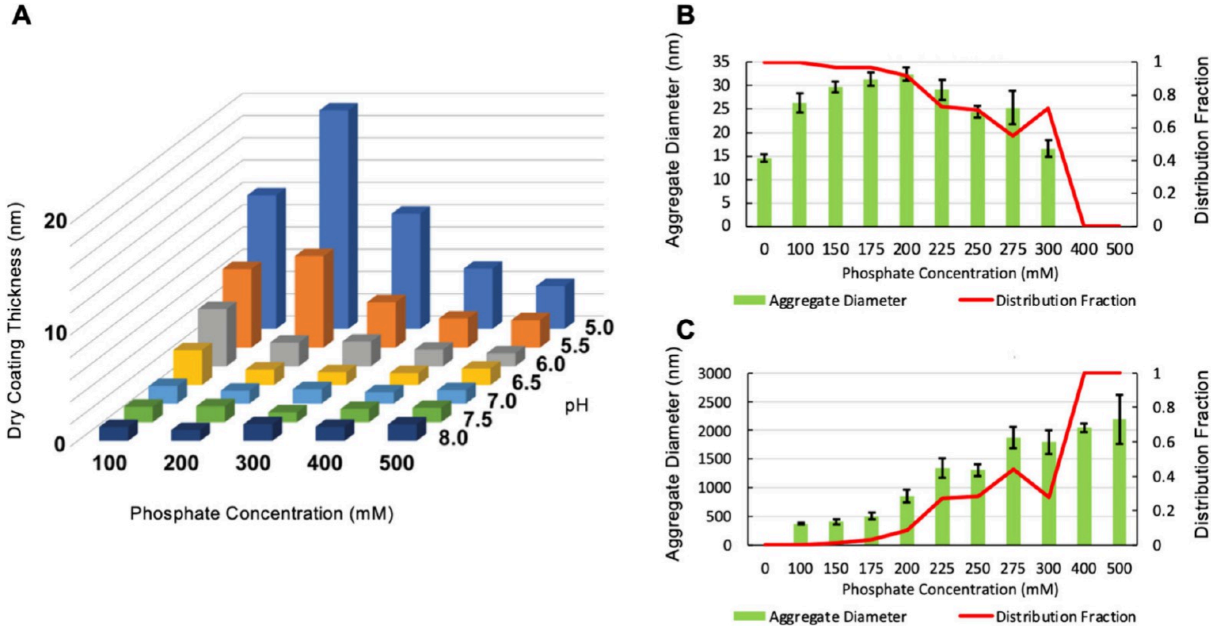

Figure 2. Investigating coating thickness and solution-phase assembly of silk fibroin at various solution pH and phosphate concentrations. (A) Spectroscopic ellipsometry measurements of silk fibroin coatings on planar TiO_2 after 24 h of coating growth; 0.5 mg/mL silk fibroin. (B and C) Dynamic light scattering measurements of silk fibroin assemblies formed at solution pH 5, 0.5 mg/mL silk fibroin. Coating solution consists of a bimodal distribution of protein assembly sizes, with the smaller population shown in B and the larger population shown in C.

subglobules from the larger globule complex. However, assuming the subglobules exhibit a half ellipsoid-like configuration on the TiO_2 surface with an average diameter of ∼30 nm and average height of ∼12 nm via AFM analysis of 5 distinct subglobules, their estimated volume is $\sim 5.65 \times 10^3$ nm^3. Assuming an estimated hydrated protein density of 0.74–0.97 g/cm^3 (assuming a swelling ratio of 1.34 by comparing the dry-state globule volume via AFM to the hydrated-state globule volume via DLS) this would suggest that the subglobules are comprised of 25–33 individual silk fibroin chains.

Coating Growth Relies on a Balance of Protein–Protein and Protein–Surface Interactions. The rate of coating formation is highly dependent on both the phosphate concentration and solution pH of the coating solution, as evidenced by coating thickness after 24 h on TiO_2 using different coating solution compositions (Figure 2A). Coatings could not be grown above pH 6.5 at any phosphate concentration, nor above a phosphate concentration of 300 mM at any solution pH. Even within a pH range of 5–6.5 and phosphate range of 100 mM – 300 mM, a regime where coating growth is facilitated, there are stark differences in coating thickness. A solution containing 200 mM phosphate at pH 5 appears to optimally facilitate coating growth. At this pH, silk fibroin is near its isoelectric point of 4.39[49] and thus has decreased protein–protein charge repulsion, as confirmed by ζ-potential analysis (Figure S3). Bare TiO_2 has a slight negative charge, so protein–surface repulsion is also decreased at pH 5, thus further facilitating adsorption. However, better coating growth at intermediate phosphate concentrations is counterintuitive, as phosphate is a kosmotropic ion that promotes protein–protein interactions and chain folding by removing the water hydration layer around protein backbones. This result suggests that the interfacial assembly of nanothin silk fibroin coatings relies on a careful balance of protein–protein and protein–surface interactions.

Solution-phase self-assembly occurs concurrently with interfacial coating growth in our system, thus we investigated the solution-phase aggregation behavior of silk fibroin under different phosphate concentrations at pH 5 via dynamic light scattering (DLS) (Figure 2B and C). In the presence of phosphate, we observe two distinct populations of silk fibroin aggregates - a small nanoscale species with a narrow size distribution that participates in coating formation as visualized by AFM (herein referred to as the “active” species), and a large heterogeneous aggregate species that does not participate in coating formation. The “active” nanoaggregates are predominantly observed at lower phosphate concentrations (100–250 mM), reaching a maximum size around 30–35 nm in diameter at 200 mM phosphate, which coincides with the optimal concentration for coating growth. At these conditions, active nanoaggregates comprise roughly 90% of the species in solution by volume. Furthermore, Figure S4 shows these active nanoaggregates only form at pH 5, where protein surface charges are minimized. Upon further increasing the phosphate concentration (>200 mM), we observe a reduction in both the diameter and the population of the active nanoaggregate, likely due to salting-out effects previously documented for silk fibroin in the presence of high phosphate concentrations.[43] The large inactive aggregates are favored at higher phosphate concentrations and are several hundred nanometers to micrometers in diameter. Both the diameter and population of this inactive species increase with phosphate concentration until all observed species in solution are inactive protein precipitates at ≥400 mM phosphate, where no coating growth is observed. Here, the kosmotropic phosphate ions likely shift the balance of interactions to favor solution-phase aggregation rather interfacial assembly, inhibiting coating formation at higher phosphate concentrations. It should be noted that our studies are performed at a silk fibroin concentration of 0.05 wt %, which is 10–100 times lower than concentrations typically explored in literature, and thus our self-assembly behavior may

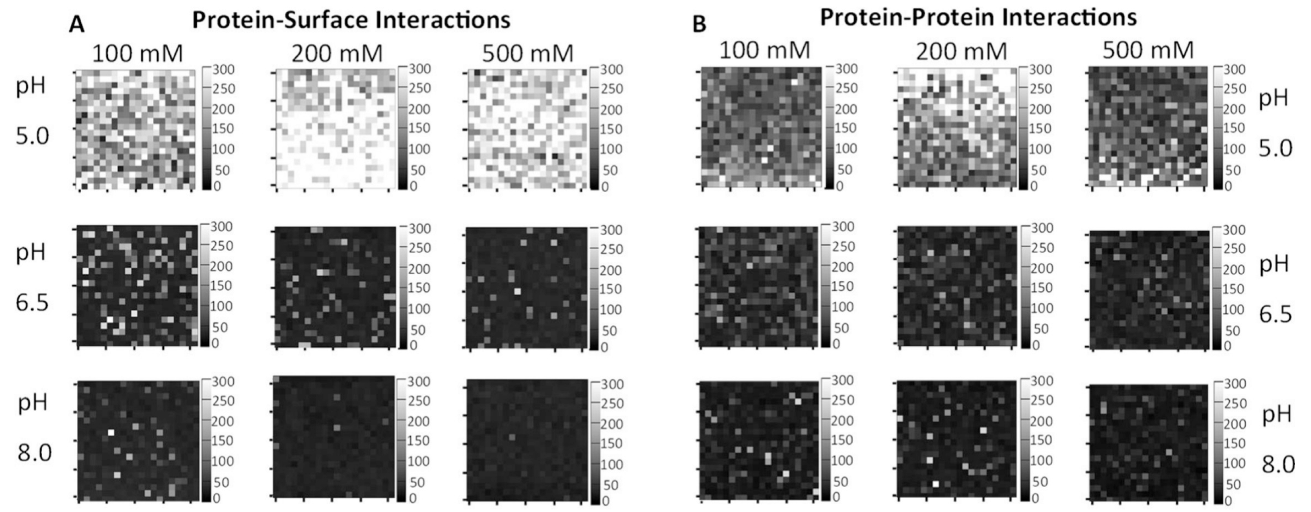

Figure 3. AFM force spectroscopy maps showing forces of (A) protein−surface interactions of a silk fibroin coated silica probe and bare TiO_2 substrate, and (B) protein−protein interactions between silk fibroin coated probe and substrate at various solution pH and phosphate concentrations. Images at 20 μm^2 with tick marks at 5 μm intervals. Scale bar represents piconewtons (pN). The highest protein−surface and protein−protein interactions are observed at the optimal coating condition (200 mM phosphate, pH 5.0). High and low force measurements are represented as white and black, respectively.

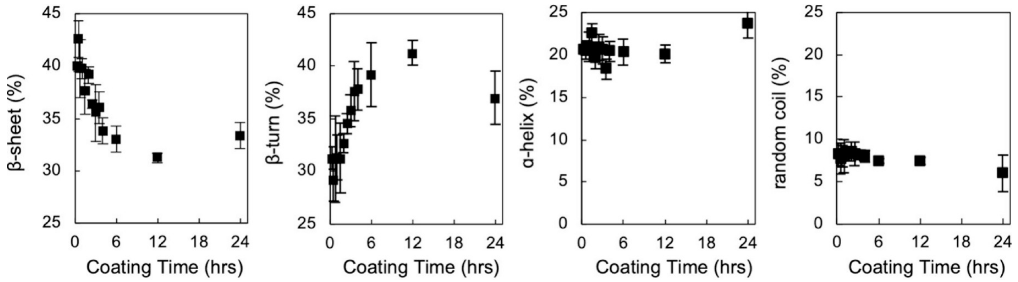

Figure 4. Secondary structure evolution of silk fibroin coatings measured by ATR-FTIR at various time points in the coating process. Band assignments are as follows: β-sheets (1616−1637, 1695−1705 cm^{-1}), random coil (1638−1655 cm^{-1}), α-helix (1656−1663 cm^{-1}), β-turns (1663−1695 cm^{-1}).

vary from previous reports where hydrogelation or nanofiber formation was observed.[50,51]

To investigate the interplay of protein−protein and protein−surface interactions during coating formation, AFM force spectroscopy measurements between a silk fibroin-coated silica particle and a bare or silk fibroin-coated TiO_2 surface were conducted. Not all previous solution pH and phosphate concentration combinations (Figure 2A) were tested, rather, solution compositions were chosen to compare the interaction strengths at the optimum coating conditions to the most extreme conditions (i.e., the highest and lowest combinations of phosphate and solution pH). Force maps generated between the silk fibroin-coated probe and bare TiO_2 are displayed in (Figure 3A) for the different conditions tested. The force maps show a clear dependence of the interaction strength between silk fibroin and TiO_2 on both solution pH and phosphate concentration, with the strongest interactions (white) observed at pH 5 and 200 mM phosphate. Protein−protein interactions measured using the same buffer conditions between the silk fibroin-coated silica particle and an existing silk fibroin coating on TiO_2 show similar trends, where the highest interactions are observed at pH 5 and 200 mM phosphate (Figure 3B). Additional analysis of AFM force measurements plotted as histogram distributions with mean and STDEV of force measurements for each of the tested conditions can be found in (Figure S5). These results support previous insights gained by DLS and suggest that pH near the isoelectric point of silk fibroin facilitates protein−protein and protein−surface interactions by reducing electrostatic repulsion, while phosphate ions play a more complex role in protein assembly in solution and at an interface. Higher phosphate concentrations may promote intramolecular or intra-aggregate interactions (e.g., hydrogen bonding, hydrophobic interactions) at the cost of intermolecular and interaggregate interactions. Alternatively, lower phosphate concentrations may not have a strong enough kosmotropic effect to promote intermolecular or intramolecular interactions at all. Continuous coating growth appears to require an intermediate phosphate concentration that balances interactions in a manner that promotes interfacial accumulation without massive solution-phase aggregation.

***β*-Sheet Formation Plays a Critical Role in Coating Growth.** The self-assembly of silk fibroin is characterized by a transition in secondary structure from being predominantly random coil to β-sheet rich, which is often experimentally triggered by kosmotropic salts or dehydrating alcohols.[21,23,52,53] We investigated the change in secondary structure of silk fibroin over time by ATR-FTIR to elucidate the intermolecular forces at play during coating formation (Figure 4). Multipeak deconvolution of the amide I region (Figure S6) between 1600 cm^{-1} - 1700 cm^{-1} show that early

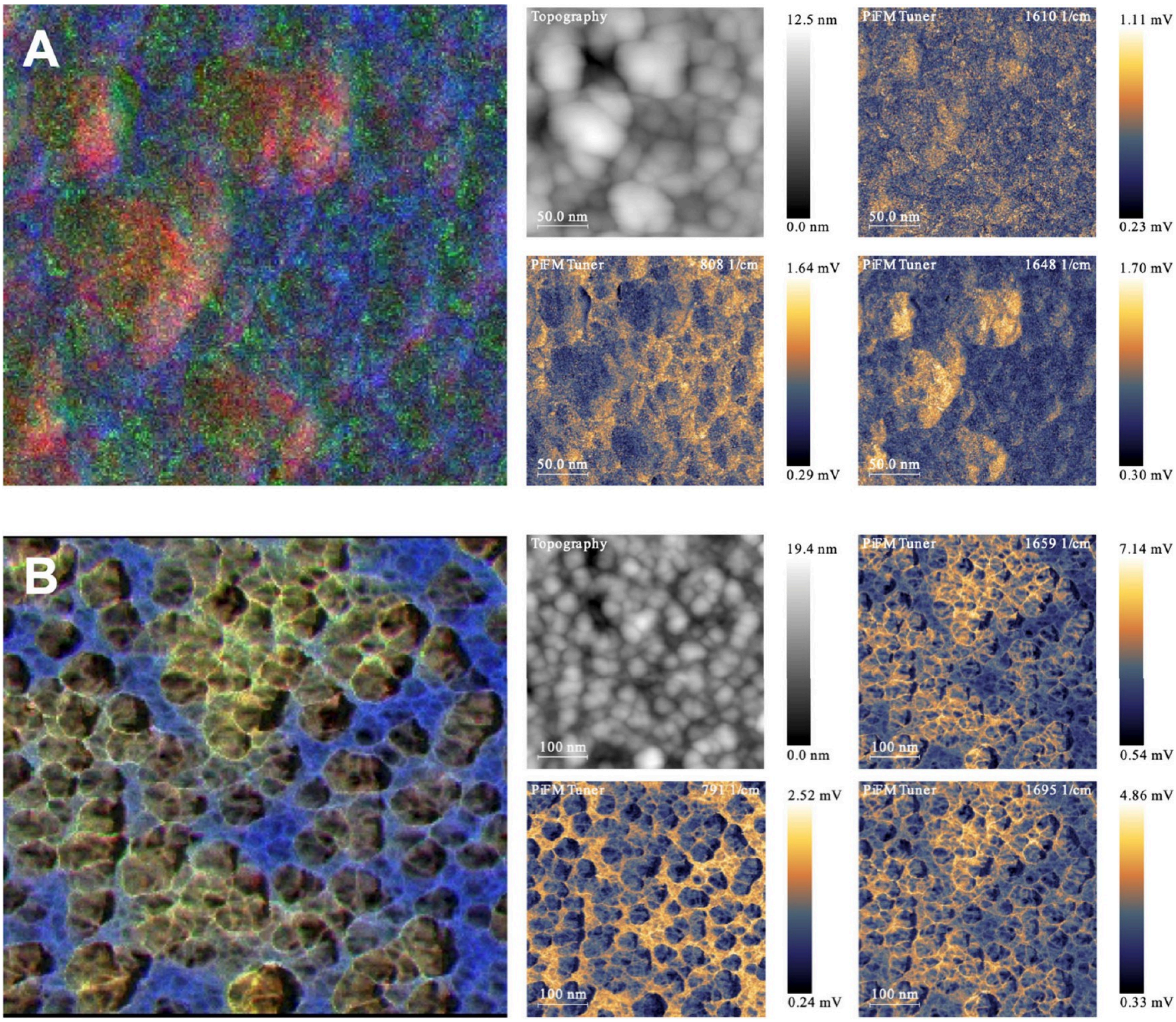

Figure 5. Infrared Photo-Induced Force Microscopy images of silk fibroin coatings formed for (A) 15 min (250 nm^2 field of view) and (B) 1.5 h (500 nm^2 field of view) with topography mapping and IR signals for individual secondary structures present in samples. IR assignments of 808 cm^{-1}, 1610 cm^{-1}, and 1648 cm^{-1} in 15 min sample correspond to TiO$_2$ (blue), β-sheet (green), and α-helix (red), respectively. IR assignments of 791 cm^{-1}, 1659 cm^{-1}, and 1695 cm^{-1} in 1.5 h sample correspond to TiO$_2$ (blue), α-helix (red), and β-sheet/turn (green), respectively.

coating time points exhibit higher β-sheet content (40.0 ± 0.4% at 15 min) compared to coatings at later time points (which stabilize at 33.3 ± 1.2% at 24 h). Over the same period, β-turn content increases from 31.3 ± 1.1% to 37.0 ± 2.5% while the α-helix and random coil contributions remain relatively constant. This result is counterintuitive, as we may expect β-sheet content to increase over time as the coatings are continuously exposed to a kosmotropic ion. Secondary structure characterization of the solution-phase silk fibroin nanoaggregates formed in 200 mM phosphate for 24 h yield β-sheet content of 30.2 ± 7.5%, which is similar to the content observed in coatings after 12 and 24 h, though the β-turn content is lower than that of the coating (Figure S7, Fitted Results Figure S8). Since the β-sheet content of the coatings decreases asymptotically toward the β-sheet content of solution-phase nanoaggregates, we can surmise that the initial stage of coating formation is dominated by absorption of a relatively β-sheet-rich species while interfacial accumulation of the nanoaggregates observed in solution dominates the later stages.

Infrared photoinduced force microscopy (PiFM) measurements were conducted on the silk fibroin coatings to investigate the spatial distribution of the secondary structures at various time points in the coating process (Figure 5A). PiFM detects infrared adsorption at nanoscale resolution using mechanical forces to measure near-field optical interactions between an AFM tip and sample.[54] After 15 min of coating time, surface-bound silk fibroin nanoglobules appear to be comprised mainly of α-helix/random coil structures (red channel, 1648 cm^{-1}), although bulk measurement of the coating via ATR-FTIR shows a much higher β-sheet content. Surprisingly, the β-sheet signal (green, 1610 cm^{-1}) appears to be homogeneously distributed across the surface rather than isolated within the silk fibroin nanoglobules. These β-sheet structures are much smaller than the silk fibroin nanoglobules and are not detectable by height or phase AFM, likely because they exist as a molecular monolayer. These small β-sheet structures may be formed by monomeric silk fibroin chains (potentially the shorter hydrolyzed fractions of the silk fibroin that results from the degumming process), which diffuse and adsorb to the surface first due to their smaller size. The rapid adsorption of a small β-sheet rich species followed by slower accumulation of relatively β-sheet poor nanoaggregates would be consistent with our ATR-FTIR results (Figure 4).

We hypothesize that the adsorbed β-sheet structures serve as anchoring points, acting as a primer layer for subsequent attachment of the nanoglobules. To test this hypothesis, we removed low molecular weight species from our silk fibroin coating solution using a 100 kDa centrifuge spin filter to compare coating kinetics with and without this primer (Figure S9). Removal of the low molecular weight species appears to reduce coating formation, suggesting that the β-sheet structures play a key role in facilitating coating growth. Solution-phase FTIR confirmed that the high molecular weight fraction, isolated as the retentate in the spin filter, has a low β-sheet and β-turn content (15.5 ± 2.2% and 14.5 ± 1.5%, respectively), which matches that of coatings formed exclusively using the high molecular weight fraction (12.5 ± 1.2% and 14.6 ± 4.3%, respectively). The low molecular weight species, isolated as the flow-through fraction in the spin filter, showed an average size of 4 nm by DLS (number-weighted average). FTIR data could not be collected due to the extremely dilute concentration of these samples. Similarly, we could not obtain an FTIR signal for coatings made using exclusively using this low molecular weight fraction, which is consistent with our expectation that this fraction comprises a small portion of the mass of our coatings. However, we observed that even though the flow-through fraction was very dilute, visible aggregates appeared within an hour after exposure to phosphate, a behavior which is not observed in the high molecular weight fraction. DLS confirmed that the average size for this low molecular weight fraction increased to 22 nm (number weighted average) after 4 h. These results suggest that the low molecular weight species is more prone to self-assembly. We performed PiFM on 15 min coatings made using exclusively the low molecular weight fraction. We observed very low signal, as expected from our prior PiFM experiments in Figure 5A showing that signal is low for areas outside of the nanoglobular aggregates, but it was apparent that the β-sheet/turn signal at 1696 cm^{-1} was generally higher than the random coil signal at 1645 cm^{-1} (Figure S9).

Silk fibroin coatings formed in 206 mM NaCl and 500 mM phosphate were also investigated using PiFM to visualize the effect of solution composition on early stage coating formation and secondary structure distribution (Figure S10). For both conditions, no β-sheet primer layer was detected, which is consistent with the lack of coating formation in these conditions. In the case of NaCl, there is likely insufficient self-assembly to promote the formation of β-sheet rich protein structures, as NaCl is not a kosmotropic salt. Virtually no surface-bound protein was observed for the 500 mM phosphate condition (data not shown). Here the solution-phase self-assembly is likely so strong that all available protein in solution forms large aggregates, as indicated by DLS (Figure 2C), rather than adsorb to the surface. It is likely that intermediate phosphate concentrations, such as 200 mM, promotes sufficient self-assembly to generate small β-sheet structures at an interface without aggregating all silk fibroin chains into large species that cannot effectively attach to the surface.

To investigate spatial distribution of secondary structures within and between neighboring surface-bound nanoglobules, a 1.5-h coating was analyzed as the substrate is nearly fully covered by protein at this time point (Figure 5B). Similar to the 15 min coating, the nanoglobules in the 1.5-h coating contain a high degree of α-helix/random coil structures. Interestingly, an enrichment of β-sheet and/or β-turn structures (1695 cm^{-1}) is observed at the interfaces between the silk fibroin nanoglobules, suggesting these secondary structures contribute to the cohesive interactions between neighboring globules. The role of hydrogen-bonded β-sheets in providing attractive interactions between silk fibroin chains is supported by a combination of DLS and Thioflavin T assay of our coating solution, which shows that the diameter of solution-phase assemblies increases proportionally with β-sheet content (Figure S11).

Coating Growth Occurs in Distinct Stages, with Kinetics that Strongly Depend on Phosphate Concentration. Quartz crystal microbalance with dissipation monitoring (QCM-D) was used to investigate silk fibroin coating kinetics in real time. Silk fibroin adsorption kinetics and coating stiffness were determined by simultaneously measuring frequency loss of the oscillating crystal (adsorbed mass) and dissipation of the shear propagating wave through the adsorbed layer (stiffness of the adsorbed layer), respectively. Mass deposition measured via QCM-D within a range of phosphate concentrations at pH 5 are displayed in Figure 6A. These results are compared with NaCl, which does not promote interfacial self-assembly. In this case, protein accumulation occurs rapidly then saturates, resulting in submonolayer coverage, as shown by dry-state AFM (Figure S12A). However, with intermediate phosphate concentrations, silk fibroin self-assembly drives interfacial accumulation past the saturation mass observed with NaCl. Here, mass accumulation initially occurs rapidly then transitions to a slower linear rate at later times. We can divide coating growth three stages: 1) an early stage, where the substrate is accessible for adsorption of solution-phase species via protein−surface

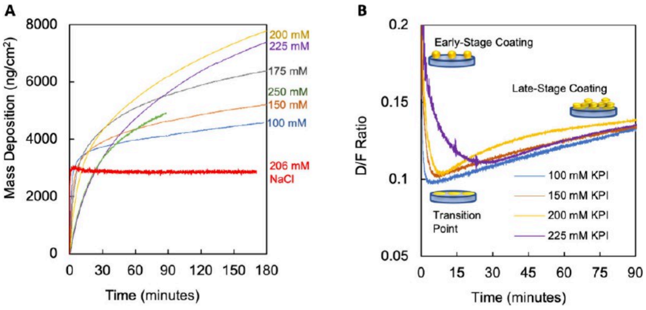

Figure 6. Silk fibroin coating kinetics and structural evolution as measured by QCM-D. (A) Silk fibroin coating kinetics in various phosphate concentrations at solution pH 5, 0.5 mg/mL silk fibroin using a standard flow module. (B) Ratio of the dissipation to frequency (D/F) of the raw QCM-D signal, showing an increase in stiffness in the early stage of coating until a maximum stiffness (lowest D/F) and subsequent softening of the protein coating over time in the late stage of coating. Graphical illustrations show hypothesized coating structure in the early and late stages of coating formation, as well as at the transition point (assumed to be where the coating is the stiffest).

interactions; 2) a late-stage, where the surface is fully covered by protein and the coating process is driven by protein−protein interactions; and 3) a transition region between the early and late stages. Lower phosphate concentrations (<175 mM) promote faster early stage and slower late-stage coating growth. Intermediate phosphate concentrations (175−225 mM) promote slower early stage kinetics but faster late-state growth. Higher phosphate concentrations (>225 mM) show both slower early stage and late-state coating growth. In agreement with our ellipsometry measurements, the optimum phosphate concentration for fast, continuous coating growth is 200 mM, where we observe slightly reduced early stage growth but the fastest rate of late-stage accumulation. In the range relevant to our studies, solution viscosity is expected to play a negligible role in silk fibroin adsorption kinetics. QCM-D and DLS experiments show a reduction in adsorption kinetics at lower protein concentrations despite a lower expected solution viscosity and smaller silk assemblies formed in solution (Figure S13). Higher protein concentrations with higher viscosities could not be evaluated within the QCM-D, as they rapidly aggregated due to the shear experienced within the tubing and slow module. The upper-bound working concentration for silk fibroin solution with 200 mM phosphate is 5 mg/mL, though this condition aggregates within the time frame of the 3-h coating experiment. Lower protein concentrations could not be evaluated by DLS due to insufficient scattering intensity below 0.1 mg/mL.

To ensure that the continuous coating growth observed via QCM-D represents protein adsorption rather than coating swelling in the hydrated environment, QCM-D was performed alongside ellipsometry in a specialized flow chamber. This data allows us to decouple dry protein mass (obtained by ellipsometry) from total hydrated mass (obtained by QCM-D). Figure S14 displays the silk fibroin dry mass deposition over time in coating solutions containing different phosphate concentrations. For all phosphate concentrations tested, except for the no-salts condition, dry mass monotonically increases over time, confirming the QCM-D data shows protein mass deposition rather than simply solvent swelling. However, due to the significant variations in flow geometry and dead volume above the substrate, the adsorption kinetics measured in the QCM-D/ellipsometry module cannot be directly compared to that of the standard flow module.

Two-Stage Modified Langmuir Kinetics Adsorption Model Mathematically Describes Coating Growth. Most existing models of protein adsorption, such as Langmuir, Random Sequential Adsorption (RSA), and Brunauer−Emmett−Teller, include a term for the maximum possible surface coverage at equilibrium ("jamming limit"), which changes with protein concentration in solution according to their isotherms.[10,55−57] Our kinetics studies show that unlike conventional protein adsorption, our self-assembled coatings do not saturate in time and instead experience linear growth at later times. While some existing empirical adsorption models may be designed to accommodate multilayer formation, such as the Freundlich or BET models,[58] they do not provide parameters that capture our two-stage coating mechanism, nor can they effectively represent the transition from early stage to late-stage coating growth.

Here, we use the Langmuir adsorption equation as a starting point to derive a model mathematically describing our coating process. In conditions that do not promote self-assembly, silk fibroin follows Langmuir-like adsorption, where mass accumulation stops after reaching saturation at submonolayer surface coverage (Figure S15A). Although our coating assembly does not meet all the criteria for true Langmuir adsorption (e.g., in our system, adsorbed species interact laterally and the adsorption process is not fully reversible), we find Langmuir better represents our data compared to RSA (Figure S15B and C) when these models are fit to silk fibroin mass flux to the surface over time in conditions that do not promote self-assembly. While erroneous conclusions can be made by interpreting protein adsorption events as Langmuir when the criteria are not satisfied,[55] we do not attempt to extract thermodynamic properties such as equilibrium constants or adsorption free energies from this model. Our modified kinetic adsorption model simply serves as a basis for separating early and late-stage coating growth rates.

We start with the original Langmuir kinetic adsorption equation

$$\frac{d\theta}{dt} = k_a c^* \left(1 - \frac{\theta}{\theta_{\max}}\right) - k_d \theta \tag{1}$$

where θ is surface coverage, θ_{max} is the maximum coverage level of the protein, $d\theta/dt$ is the change in surface coverage of the underlying substrate over time, $c*$ is the effective concentration of the bulk protein solution above the surface, and k_a and k_d are the adsorption and desorption rate constants, respectively. Assuming mass deposition is proportional to surface coverage in the early stages of adsorption, we replace surface coverage with total specific mass deposition in the model, yielding:

$$\frac{dM}{dt} = k_a c^* \left(1 - \frac{M}{M_{\max}}\right) - k_d M \tag{2}$$

The term dM/dt is the change in specific mass over time representing protein flux to the surface, M is mass deposited on the QCM-D sensor, and M_{max} is a free fit parameter representing the maximum mass deposited on the QCM-D sensor. To capture our linear late-stage coating growth, a new parameter, k_{ss}, is introduced to represent silk fibroin adsorption to surface-bound silk assemblies (protein−protein interactions). To avoid overfitting the data, the desorption term was removed as desorption of silk fibroin after coating formation was experimentally shown to be negligible (Figure S15A).

$$\frac{dM}{dt} = k_a c^* \left(1 - \frac{M}{M_{\max}}\right) + k_{ss} \tag{3}$$

The first part of the equation, which resembles the original Langmuir kinetic adsorption equation, represents protein−surface interactions. However, as the surface becomes completely covered with protein globules (Figure 1), the effect of the surface on adsorbing proteins diminishes. Here, we introduce an exponential function with a fitted time constant (β) multiplied by time (t) to extinguish the protein−surface interaction term as the coating approaches full surface coverage, yielding

$$\frac{dM}{dt} = \frac{k_a c^* \left(1 - \frac{M}{M_{\max}}\right)}{e^{\beta t}} + k_{ss} \tag{4}$$

As the protein−surface interaction term is extinguished, the model smoothly converges to the k_{ss} term, describing late-stage

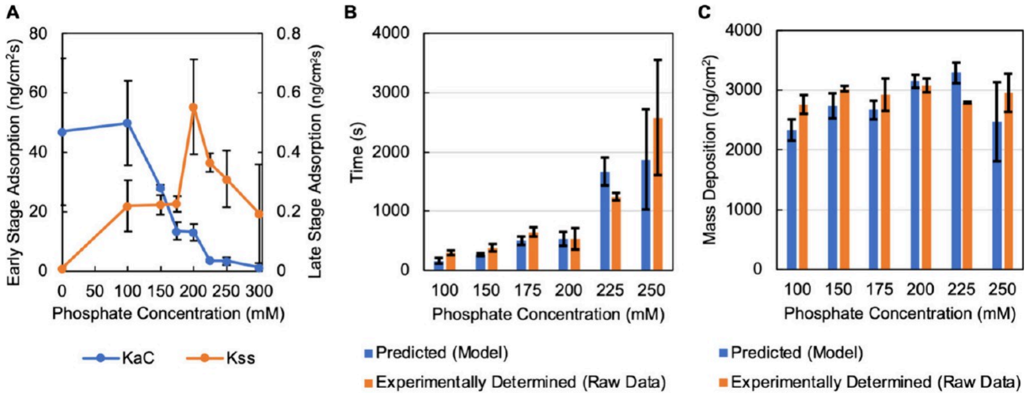

Figure 7. (A) Early- and late-stage coating adsorption rate constants extracted from fits of QCM kinetics data to the modified adsorption model (eq 4). (B) Predicted transition time point occurring during coating process as experimentally determined from D/F ratio (orange) compared to transition time point predicted by eq 4. (C) Total mass deposition on the QCM-D sensor at the transition point experimentally determined (orange) and predicted by eq 4 (blue).

coating growth governed entirely by protein−protein interactions.

Taking the derivative of our coating kinetics curves produced by QCM-D yields protein flux (ng/cm^{2}s) to the surface over time, allowing us to fit our model to the data and extract early- and late-stage adsorption rate constants, k_a (ng/cm^{2}sM) and k_{ss} (ng/cm^{2}s), respectively, where M represents molarity in the k_a constant. Since we continuously replenish our concentration boundary layer in a QCM-D flow module, we assume c^* to be constant and consider the full term $k_a c^*$ to be our early stage adsorption rate constant. This allows for direct comparison between early- and late-stage adsorption rate constants as they are both in units of (ng/cm^{2}s). Figure 7A shows the early- and late-stage adsorption rate constants derived from fitting our modified eq 4 to the QCM-D data (Figure 6A) as a function of phosphate concentration (Model Fits and Residuals, see Figure S16). The early stage adsorption rate constant, $k_a c^*$, is maximized at low phosphate concentration, then steadily decreases as phosphate concentration is increased, suggesting that protein−protein assembly negatively impacts the rate of protein−surface adsorption in the initial stages of coating formation. Conversely, the late-stage adsorption rate constant, k_{ss}, increases with phosphate concentration until the optimum coating concentration (200 mM) is reached. However, further increasing phosphate concentration decreases k_{ss}, suggesting that high phosphate concentrations negatively impact interfacial accumulation regardless of whether it is driven by protein−protein or protein−surface interactions. These fitted results support the DLS results, which show that low phosphate concentrations do not adequately promote self-assembly, thus leading to more conventional adsorption behavior with minimal late-stage growth, while high phosphate concentrations generate mostly large solution-phase that cannot attach to the surface.

Structure Change Marks the Transition between Early- and Late-Stage Coating Growth. To understand the relationship between early and late-stage coating growth, we define a "transition point" where the coating mechanism shifts from being predominantly dependent on protein−surface interactions to protein−protein interactions. To understand this transition, the dissipation-to-frequency (D/F) ratio over time was analyzed from the raw data, which measures the loss of energy through the coating (D) as a function of mass deposited on the surface (F). This ratio gives insight into structural properties of the silk fibroin coating as it forms. A low D/F ratio represents a stiff coating, whereas a high D/F ratio represents a softer coating. To this end, a D/F ratio of lower than 0.05−0.1 is defined as a rigid coating, whereas a value above 0.1 is considered soft. The magnitude of the D/F ratios of our silk fibroin coatings indicate a soft, hydrogel like coating (Figure 6B), which is supported by liquid-mode AFM imaging (Figure 1C). In the early stages of coating growth, the coating starts very soft (high D/F ratio), but then rapidly stiffens. The minimum in the D/F ratio can be interpreted as the time point in which the coating is at its stiffest, representing a more rigidly bound interfacial layer that is possibly due to protein spreading, a commonly observed phenomenon.[55,57,59,60] After this point, the coating slowly becomes softer as more nanoaggregates accumulate on the existing silk layer rather than the substrate surface during late-stage coating growth. Since the time at which this D/F minimum occurs depends on phosphate concentration, we consider this minimum in the D/F ratio to be the transition point between the early- and late-stage adsorption regions.

Figure 7B and C displays the time point and surface mass deposition corresponding to the minimal D/F ratio. As phosphate concentration increases, the time when the minimal D/F is observed also increases, indicating a slower protein−surface adsorption when more phosphate is present (Figure 7B). However, the total mass absorbed to the surface at this transition point for all phosphate concentrations tested lies in a narrow range from 2750 to 3100 ng/cm^2, despite occurring at different time points for each coating condition (Figure 7C). Comparing these values to the NaCl sample, which undergoes protein−surface adsorption then rapid saturation without further growth, the mass accumulated at the transition point is nearly identical to the mass accumulated at the point of saturation in NaCl (∼3000 ng/cm^2, Figure 6A, red). This finding suggests that the transition between the early and late-stage coating growth occurs at the apparent "jamming limit" of protein adsorption without the influence of self-assembly. At the "jamming limit", all accessible surface binding sites are effectively occupied, and without attractive interspecies interactions, protein adsorption is expected to reach equilibrium. However, in our system, silk fibroin can surpass this common limitation of protein adsorption and continuously accumulate at the interface via protein−protein interactions at optimal phosphate concentrations.

We demonstrated the utility of our model by predicting when the transition between early stage and late-stage coating growth occurs, which we hypothesize to be represented by the inverse time constant ($1/\beta$) in our model. We compared $1/\beta$ from our fitted data to our experimentally determined transition point, which is where D/F is minimized. Figure 7B shows that the predicted transition time aligns closely with experimentally determined values. Additionally, the total masses accumulated on the surface at these predicted times fall within the range of 2300−3300 ng/cm^2, which is in close agreement with experimentally determined values of mass accumulated at the transition point (Figure 7C). We also utilize our model to quantify variations in coating kinetics when alterations are made to the coating process. As discussed previously, Figure S9 shows a reduction in overall coating formation when the smallest population in the coating solution, the species likely responsible for the β-sheet primer layer, is removed by centrifuge spin filters. Here we find that the early stage adsorption rate constant decreases from 13.1 to 5.5 ng/cm^{2}s, a 58% decrease, while the late-stage adsorption rate constant decreases 25% from 0.55 to 0.41 ng/cm^{2}s.

Self-Assembled Silk Fibroin Coating Provide a Facile "Universal" Method for Enhancing Surface Functionality. Previous work in our lab has demonstrated that our silk fibroin coatings can be used functionalize high aspect ratio poly-L-lactic acid (PLLA) scaffolds for enhanced nerve tissue regeneration.[16] To highlight the versatility of our self-assembled coatings, we explored coating properties and stability on a variety of substrates and in a variety of solvents. Figure 8A shows static water contact angle measurements on a variety of surfaces with and without silk coatings. Regardless of the underlying properties of the substrates (e.g., hydrophobic, hydrophilic, organic, inorganic), the coated substrates exhibit a narrow distribution of water contact angles that correspond to the contact angle of bulk silk fibroin, which suggests the ability of our coatings to completely cover a wide range of surfaces. Our coatings are tenaciously bound to surfaces, owing to a multiplexing of adhesive interactions by lateral attractive forces within the coating. Figure S17 shows that these coatings are stable (e.g., no delamination or dissolution) in a variety of harsh solution conditions such as ethanol, toluene, and dichloromethane, and physiologically relevant buffers such as MOPS and phosphate buffer. The high packing density of surface-bound nanoglobules (Figure 1F) suggests the potential for these silk fibroin coatings to act as nonfouling surfaces. Using QCM-D, Figure 8B shows that a silk fibroin coating formed on a TiO_2 sensor can reduce bovine serum albumin (BSA) adsorption by ∼85% when compared to a bare TiO_2 surface under identical conditions (Figure 8B, inset) at low BSA concentrations. An antifouling study was additionally conducted at a higher BSA concentration (10 mg/mL) on silica resin, where adsorption of FITC-labeled BSA was imaged on both silk fibroin-coated and bare resin (Figure 8C and D). We observe less overall FITC-BSA adsorption onto the silk-coated resin, demonstrating the nanothin silk fibroin coating can prevent BSA fouling on nonplanar surfaces in biologically relevant serum protein concentrations. The ability of silk fibroin to act as a nonfouling surface likely stems from the density of silk fibroin nanoglobules on the surface, leaving no available surface area for unwanted protein adsorption. Additionally, these hydrogel-like silk fibroin coatings are expected to retain bound water, contributing entropic and osmotic repulsive forces to approaching proteins such as BSA.[61]

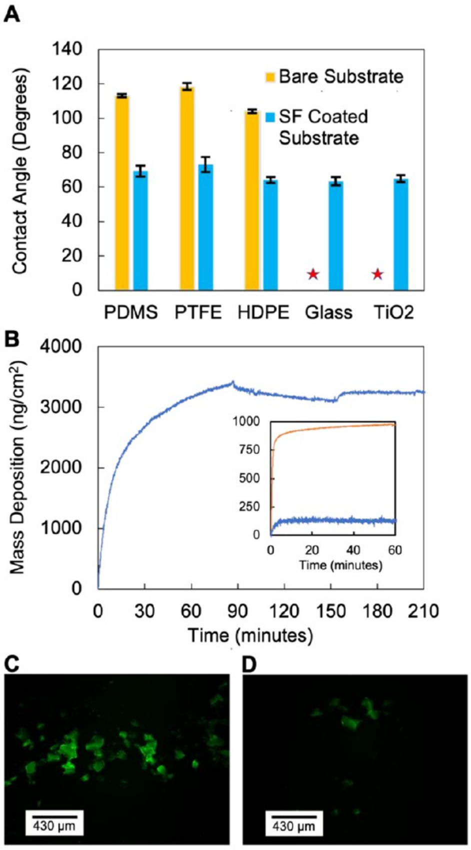

Figure 8. Evaluating the potential of silk fibroin self-assembled coatings as a noncovalent surface modification strategy. (A) Contact angle measurements on hydrophobic and hydrophilic materials with (blue) and without (yellow) silk fibroin coatings. Substrates marked with a star symbol are fulling wetted without the silk fibroin coating. (B) QCM-D measurement demonstrating potential of silk coatings as a nonfouling surface. Inset compares BSA adsorption on a bare TiO_2 sensor (orange) and a silk fibroin-coated TiO_2 sensor (blue) (C and D) Fluorescent microscopy images of FITC tagged bovine serum albumin physically adsorbed to (C) bare silica and (D) silk fibroin coated silica, showing decreased nonspecific adsorption onto silk-coated silica.

■ CONCLUSIONS AND FUTURE WORK

Protein fouling of surfaces is typically considered a persistent and unavoidable problem. However, our work demonstrates that fouling by silk fibroin under conditions that balance attractive protein−protein and protein−surface interactions can be leveraged as a robust "universal" method for surface modification. We show that when silk fibroin self-assembly is triggered by an optimal concentration of potassium phosphate, adherent defect-free coatings can be continuously grown at a solid−liquid interface without requiring covalent cross-linking or specialized adhesion motifs. These coatings readily transform the physicochemical properties of a variety of hydrophobic and hydrophilic surfaces and are stable against exposure to aqueous and organic solvents. Our studies show that coating formation by silk fibroin is a two-stage process wherein nanoaggregates formed in solution first adhere to the substrate, then adhere to existing surface-bound silk fibroin. Thus, unlike conventionally described fouling phenomena, self-assembly occurs alongside adsorption and accumulation of silk fibroin does not saturate over time. Coating formation is highly dependent on phosphate concentration and solution pH. Coating growth only occurs near the isoelectric point of silk fibroin with an intermediate phosphate concentration (approximately 200 mM). Here, electrostatic repulsion is minimized and supramolecular β-sheet formation, which underlies cohesive interactions within the coating, is promoted without encountering large-scale solution-phase aggregation. A primer layer consisting of low molecular weight β-sheet rich species adsorbs in the initial stages of coating formation and facilitates coating growth. Because current models of protein adsorption do not adequately represent our two-stage interfacial process, we present a new kinetic model that combines a Langmuir-like adsorption equation at early times with continuous linear growth at later times.

Silk fibroin coating growth may have parallels to other natural interfacial phenomena, such as mussel bioadhesion or biofilm formation, wherein biomacromolecules interact non-specifically with surfaces while supramolecular assembly connects multiple adhesive interactions that may be individually weak. Thus, future work should explore this coating growth process with other biomacromolecules capable of self-assembly, such as elastin-like polypeptides or amyloid proteins. The exact molecular mechanism by which phosphate controls silk fibroin self-assembly remains unclear, as it may have protein-specific effects in addition to being a kosmotropic ion. Future work should explore specific protein-ion effects by investigating more and less kosmotropic salts from the Hofmeister series on silk fibroin interfacial assembly.

■ ASSOCIATED CONTENT

Supporting Information

The Supporting Information is available free of charge at https://pubs.acs.org/doi/10.1021/acsami.4c07528.

> Additional data and analysis of dynamic light scattering, zeta potential, photoinduced force microscopy, FTIR, QCM-D, ThT, and AFM force spectroscopy results (PDF)

■ AUTHOR INFORMATION

Corresponding Author

R. Helen Zha − *Department of Chemical and Biological Engineering, 110 Eighth Street, Rensselaer Polytechnic Institute, Troy, New York 12180, United States; Center for Biotechnology and Interdisciplinary Studies, Rensselaer Polytechnic Institute, Troy, New York 12180, United States;* orcid.org/0000-0002-0766-5705; Email: zhar@rpi.edu

Authors

Caleb Wigham − *Department of Chemical and Biological Engineering, 110 Eighth Street, Rensselaer Polytechnic Institute, Troy, New York 12180, United States; Center for Biotechnology and Interdisciplinary Studies, Rensselaer Polytechnic Institute, Troy, New York 12180, United States;* orcid.org/0000-0003-4836-2759

Tanner D. Fink − *Department of Chemical and Biological Engineering, 110 Eighth Street, Rensselaer Polytechnic Institute, Troy, New York 12180, United States; Center for Biotechnology and Interdisciplinary Studies, Rensselaer Polytechnic Institute, Troy, New York 12180, United States;* orcid.org/0000-0003-2102-3220

Mirco Sorci − *Center for Biotechnology and Interdisciplinary Studies, Rensselaer Polytechnic Institute, Troy, New York 12180, United States;* orcid.org/0000-0001-6053-6702

Padraic O'Reilly − *Molecular Vista, San Jose, California 95119, United States*

Sung Park − *Molecular Vista, San Jose, California 95119, United States*

Jeongae Kim − *Department of Chemical and Biological Engineering, 110 Eighth Street, Rensselaer Polytechnic Institute, Troy, New York 12180, United States; Center for Biotechnology and Interdisciplinary Studies, Rensselaer Polytechnic Institute, Troy, New York 12180, United States*

Vrushali R. Varude − *Department of Chemical and Biological Engineering, 110 Eighth Street, Rensselaer Polytechnic Institute, Troy, New York 12180, United States; Center for Biotechnology and Interdisciplinary Studies, Rensselaer Polytechnic Institute, Troy, New York 12180, United States;* orcid.org/0009-0006-9155-5942

Complete contact information is available at: https://pubs.acs.org/10.1021/acsami.4c07528

Author Contributions

+C.W. and T.D.F. contributed equally to this work. C.W. conducted all DLS, QCM, and hydrated-FTIR experiments along with the following analysis and curve fitting. T.D.F. conducted AFM imaging, dry-state ellipsometry, dry-state FTIR, goniometer, and fluorescence microscopy experiments and subsequent analysis. V.R.V. conducted solution-phase and dry-state FTIR. M.S. conducted AFM force measurements with help from T.D.F. P.O, S.P, and V.R.V. conducted PiFM experiments. J.K. conducted stability studies with subsequent ellipsometry analysis. R.H.Z. conceptualized experiments, assisted with data analysis, and edited the manuscript.

Notes

The authors declare no competing financial interest.

■ ACKNOWLEDGMENTS

For the use of the QCM-D we thank Prof. Georges Belfort, for use of the goniometer we thank Dr. Richard Gross, and for use of the fluorescent microscope we thank Prof. Todd Przybycien. We thank Dr. Joel Morgan and the CBIS Analytical Biochemistry Core for their assistance with FTIR, Dr. Sergey Pryshchep and the CBIS Microscopy Core for their assistance with AFM and PiFM, and Dr. Sarah An and the cMDIS for their assistance with dry-state ellipsometry. We thank Dr. Dmytro Nykypanchuk and the Center for Functional Nanomaterials at Brookhaven National Lab for use of the Cypher VRS AFM. We acknowledge funding from by the National Science Foundation (NSF DMR #2045510 and DMR #2215905).

■ REFERENCES

(1) Nakanishi, K.; Sakiyama, T.; Imamura, K. On the Adsorption of Proteins on Solid Surfaces, a Common but Very Complicated Phenomenon. *J. Biosci Bioeng* **2001**, *91* (3), 233−244.

(2) Ma, Z.; Gao, C.; Gong, Y.; Shen, J. Cartilage Tissue Engineering PLLA Scaffold with Surface Immobilized Collagen and Basic Fibroblast Growth Factor. *Biomaterials* **2005**, *26* (11), 1253−1259.

(3) He, L.; Tang, S.; Prabhakaran, M. P.; Liao, S.; Tian, L.; Zhang, Y.; Xue, W.; Ramakrishna, S. Surface Modification of PLLA Nano-scaffolds with Laminin Multilayer by LbL Assembly for Enhancing Neurite Outgrowth. *Macromol. Biosci* **2013**, *13* (11), 1601−1609.

(4) Gu, J.; Su, Y.; Liu, P.; Li, P.; Yang, P. An Environmentally Benign Antimicrobial Coating Based on a Protein Supramolecular Assembly. *Acs Appl. Mater. Inter* **2017**, *9* (1), 198−210.

(5) Pangule, R. C.; Brooks, S. J.; Dinu, C. Z.; Bale, S. S.; Salmon, S. L.; Zhu, G.; Metzger, D. W.; Kane, R. S.; Dordick, J. S. Antistaphylococcal Nanocomposite Films Based on Enzyme-Nanotube Conjugates. *ACS Nano* **2010**, *4* (7), 3993−4000.

(6) Goli, K. K.; Rojas, O. J.; Genzer, J. Formation and Antifouling Properties of Amphiphilic Coatings on Polypropylene Fibers. *Biomacromolecules* **2012**, *13* (11), 3769−3779.

(7) Wu, Z.; Yang, P. Simple Multipurpose Surface Functionalization by Phase Transited Protein Adhesion. *Adv. Mater. Interfaces* **2015**, *2* (2), 1400401.

(8) Adamczyk, Z. Protein Adsorption: A Quest for a Universal Mechanism. *Curr. Opin Colloid In* **2019**, *41*, 50−65.

(9) Talbot, J.; Tarjus, G.; Tassel, P. R. V.; Viot, P. From Car Parking to Protein Adsorption: An Overview of Sequential Adsorption Processes. *arXiv*, 1999, DOI: 10.48550/arxiv.cond-mat/9906428.

(10) Rabe, M.; Verdes, D.; Seeger, S. Understanding Protein Adsorption Phenomena at Solid Surfaces. *Adv. Colloid Interfac* **2011**, *162* (1−2), 87−106.

(11) Vogler, E. A. Protein Adsorption in Three Dimensions. *Biomaterials* **2012**, *33* (5), 1201−1237.

(12) Asanov, A. N.; Delucas, L. J.; Oldham, P. B.; Wilson, W. W. Interfacial Aggregation of Bovine Serum Albumin Related to Crystallization Conditions Studied by Total Internal Reflection Fluorescence. *J. Colloid Interface Sci.* **1997**, *196* (1), 62−73.

(13) Solomonov, A.; Shimanovich, U. Self-Assembly in Protein-Based Bionanomaterials. *Israel J. Chem.* **2020**, *60* (12), 1152−1170.

(14) Altman, G. H.; Diaz, F.; Jakuba, C.; Calabro, T.; Horan, R. L.; Chen, J.; Lu, H.; Richmond, J.; Kaplan, D. L. Silk-Based Biomaterials. *Biomaterials* **2003**, *24* (3), 401−416.

(15) Vepari, C.; Kaplan, D. L. Silk as a Biomaterial. *Prog. Polym. Sci.* **2007**, *32* (8−9), 991−1007.

(16) Ziemba, A. M.; Fink, T. D.; Crochiere, M. C.; Puhl, D. L.; Sapkota, S.; Gilbert, R. J.; Zha, R. H. Coating Topologically Complex Electrospun Fibers with Nanothin Silk Fibroin Enhances Neurite Outgrowth in Vitro. *Acs Biomater Sci. Eng.* **2020**, *6* (3), 1321−1332.

(17) Fink, T. D.; Funnell, J. L.; Gilbert, R. J.; Zha, R. H. One-Pot Assembly of Drug-Eluting Silk Coatings with Applications for Nerve Regeneration. *ACS Biomater. Sci. Eng.* **2024**, *10* (1), 482−496.

(18) Zha, R. H.; Delparastan, P.; Fink, T. D.; Bauer, J.; Scheibel, T.; Messersmith, P. B. Universal Nanothin Silk Coatings via Controlled Spidroin Self-Assembly. *Biomater Sci-uk* **2019**, *7*, 683.

(19) Andersson, M.; Chen, G.; Otikovs, M.; Landreh, M.; Nordling, K.; Kronqvist, N.; Westermark, P.; Jörnvall, H.; Knight, S.; Ridderstråle, Y.; Holm, L.; Meng, Q.; Jaudzems, K.; Chesler, M.; Johansson, J.; Rising, A. Carbonic Anhydrase Generates CO2 and H+ That Drive Spider Silk Formation Via Opposite Effects on the Terminal Domains. *Plos Biol.* **2014**, *12* (8), No. e1001921.

(20) Dicko, C.; Kenney, J. M.; Knight, D.; Vollrath, F. Transition to a β-Sheet-Rich Structure in Spidroin in Vitro: The Effects of PH and Cations†. *Biochemistry-us* **2004**, *43* (44), 14080−14087.

(21) Lammel, A. S.; Hu, X.; Park, S.-H.; Kaplan, D. L.; Scheibel, T. R. Controlling Silk Fibroin Particle Features for Drug Delivery. *Biomaterials* **2010**, *31* (16), 4583−4591.

(22) Gopalakrishnan, S.; Xu, J.; Zhong, F.; Rotello, V. M. Strategies for Fabricating Protein Films for Biomaterial Applications. *Adv. Sustain Syst* **2021**, *5* (1), 2000167.

(23) Wang, X.; Kim, H. J.; Xu, P.; Matsumoto, A.; Kaplan, D. L. Biomaterial Coatings by Stepwise Deposition of Silk Fibroin. *Langmuir* **2005**, *21* (24), 11335−11341.

(24) Nilebäck, L.; Hedin, J. N.; Widhe, M.; Floderus, L. S.; Krona, A.; Bysell, H.; Hedhammar, M. Self-Assembly of Recombinant Silk as a Strategy for Chemical-Free Formation of Bioactive Coatings - a Real-Time Study. *Biomacromolecules* **2017**, *18*, 846.

(25) Malay, A. D.; Suzuki, T.; Katashima, T.; Kono, N.; Arakawa, K.; Numata, K. Spider Silk Self-Assembly via Modular Liquid-Liquid Phase Separation and Nanofibrillation. *Sci. Adv.* **2020**, *6* (45), No. eabb6030.

(26) Knight, D. P.; Vollrath, F. Changes in Element Composition along the Spinning Duct in a Nephila Spider. *Naturwissenschaften* **2001**, *88* (4), 179−182.

(27) Oktaviani, N. A.; Matsugami, A.; Hayashi, F.; Numata, K. Ion Effects on the Conformation and Dynamics of Repetitive Domains of a Spider Silk Protein: Implications for Solubility and β-Sheet Formation. *Chem. Commun.* **2019**, *55* (66), 9761−9764.

(28) Stengel, D.; Saric, M.; Johnson, H. R.; Schiller, T.; Diehl, J.; Chalek, K.; Onofrei, D.; Scheibel, T.; Holland, G. P. Tyrosine's Unique Role in the Hierarchical Assembly of Recombinant Spider Silk Proteins: From Spinning Dope to Fibers. *Biomacromolecules* **2023**, *24*, 1463.

(29) Slotta, U.; Tammer, M.; Kremer, F.; Koelsch, P.; Scheibel, T. Structural Analysis of Spider Silk Films. *Supramol Chem.* **2006**, *18* (5), 465−471.

(30) Humenik, M.; Smith, A. M.; Arndt, S.; Scheibel, T. Ion and Seed Dependent Fibril Assembly of a Spidroin Core Domain. *J. Struct Biol.* **2015**, *191* (2), 130−138.

(31) Jin, H.-J.; Kaplan, D. L. Mechanism of Silk Processing in Insects and Spiders. *Nature* **2003**, *424* (6952), 1057.

(32) Bucciarelli, A.; Mulloni, V.; Maniglio, D.; Pal, R. K.; Yadavalli, V. K.; Motta, A.; Quaranta, A. A Comparative Study of the Refractive Index of Silk Protein Thin Films towards Biomaterial Based Optical Devices. *Opt Mater.* **2018**, *78*, 407−414.

(33) Hu, X.; Kaplan, D.; Cebe, P. Determining Beta-Sheet Crystallinity in Fibrous Proteins by Thermal Analysis and Infrared Spectroscopy. *Macromolecules* **2006**, *39* (18), 6161−6170.

(34) A-Hassan, E.; Heinz, W. F.; Antonik, M. D.; D'Costa, N. P.; Nageswaran, S.; Schoenenberger, C.-A.; Hoh, J. H. Relative Microelastic Mapping of Living Cells by Atomic Force Microscopy. *Biophys. J.* **1998**, *74* (3), 1564−1578.

(35) ROTSCH, C.; BRAET, F.; WISSE, E.; RADMACHER, M. AFM IMAGING AND ELASTICITY MEASUREMENTS ON LIVING RAT LIVER MACROPHAGES. *Cell Biol. Int.* **1997**, *21* (11), 685−696.

(36) Sorci, M.; Dassa, B.; Liu, H.; Anand, G.; Dutta, A. K.; Pietrokovski, S.; Belfort, M.; Belfort, G. Oriented Covalent Immobilization of Antibodies for Measurement of Intermolecular Binding Forces between Zipper-Like Contact Surfaces of Split Inteins. *Anal. Chem.* **2013**, *85* (12), 6080−6088.

(37) Voinova, M. V.; Rodahl, M.; Jonson, M.; Kasemo, B. Viscoelastic Acoustic Response of Layered Polymer Films at Fluid-Solid Interfaces: Continuum Mechanics Approach. *Phys. Scr.* **1999**, *59* (5), 391−396.

(38) Greving, I.; Cai, M.; Vollrath, F.; Schniepp, H. C. Shear-Induced Self-Assembly of Native Silk Proteins into Fibrils Studied by Atomic Force Microscopy. *Biomacromolecules* **2012**, *13* (3), 676−682.

(39) Rockwood, D. N.; Preda, R. C.; Yücel, T.; Wang, X.; Lovett, M. L.; Kaplan, D. L. Materials Fabrication from Bombyx Mori Silk Fibroin. *Nat. Protoc* **2011**, *6* (10), 1612.

(40) Parent, L. R.; Onofrei, D.; Xu, D.; Stengel, D.; Roehling, J. D.; Addison, J. B.; Forman, C.; Amin, S. A.; Cherry, B. R.; Yarger, J. L.; Gianneschi, N. C.; Holland, G. P. Hierarchical Spidroin Micellar Nanoparticles as the Fundamental Precursors of Spider Silks. *Proc. National Acad. Sci.* **2018**, *115* (45), 11507.

(41) Foo, C. W. P.; Bini, E.; Hensman, J.; Knight, D. P.; Lewis, R. V.; Kaplan, D. L. Role of PH and Charge on Silk Protein Assembly in Insects and Spiders. *Appl. Phys.* **2006**, *82* (2), 223−233.

(42) Wang, Q.; Ling, S.; Yao, Q.; Li, Q.; Hu, D.; Dai, Q.; Weitz, D. A.; Kaplan, D. L.; Buehler, M. J.; Zhang, Y. Observations of 3 Nm Silk Nanofibrils Exfoliated from Natural Silkworm Silk Fibers. *Acs Mater. Lett.* **2020**, *2*, 153−160.

(43) Rammensee, S.; Slotta, U.; Scheibel, T.; Bausch, A. R. Assembly Mechanism of Recombinant Spider Silk Proteins. *Proc. National Acad. Sci.* **2008**, *105* (18), 6590−6595.

(44) Heim, M.; Römer, L.; Scheibel, T. Hierarchical Structures Made of Proteins. The Complex Architecture of Spider Webs and

Their Constituent Silk Proteins. *Chem. Soc. Rev.* **2010**, *39* (1), 156−164.

(45) Römer, L.; Scheibel, T. The Elaborate Structure of Spider Silk: Structure and Function of a Natural High Performance Fiber. *Prion* **2008**, *2* (4), 154−161.

(46) Zhong, J.; Liu, X.; Wei, D.; Yan, J.; Wang, P.; Sun, G.; He, D. Effect of Incubation Temperature on the Self-Assembly of Regenerated Silk Fibroin: A Study Using AFM. *Int. J. Biol. Macromol.* **2015**, *76*, 195−202.

(47) Oroudjev, E.; Soares, J.; Arcidiacono, S.; Thompson, J. B.; Fossey, S. A.; Hansma, H. G. Segmented Nanofibers of Spider Dragline Silk: Atomic Force Microscopy and Single-Molecule Force Spectroscopy. *Proc. National Acad. Sci.* **2002**, *99* (suppl_2), 6460−6465.

(48) Lawrence, B. D.; Wharram, S.; Kluge, J. A.; Leisk, G. G.; Omenetto, F. G.; Rosenblatt, M. I.; Kaplan, D. L. Effect of Hydration on Silk Film Material Properties. *Macromol. Biosci* **2010**, *10* (4), 393−403.

(49) Leal-Egaña, A.; Scheibel, T. Interactions of Cells with Silk Surfaces. *J. Mater. Chem.* **2012**, *22* (29), 14330−14336.

(50) Xu, D.; Guo, C.; Holland, G. P. Probing the Impact of Acidification on Spider Silk Assembly Kinetics. *Biomacromolecules* **2015**, *16* (7), 2072−2079.

(51) Floren, M.; Migliaresi, C.; Motta, A. Processing Techniques and Applications of Silk Hydrogels in Bioengineering. *J. Funct. Biomater.* **2016**, *7* (3), 26.

(52) Wang, X.; Hu, X.; Daley, A.; Rabotyagova, O.; Cebe, P.; Kaplan, D. L. Nanolayer Biomaterial Coatings of Silk Fibroin for Controlled Release. *J. Controlled Release* **2007**, *121* (3), 190−199.

(53) Huemmerich, D.; Slotta, U.; Scheibel, T. Processing and Modification of Films Made from Recombinant Spider Silk Proteins. *Appl. Phys.* **2006**, *82* (2), 219−222.

(54) Sifat, A. A.; Jahng, J.; Potma, E. O. Photo-Induced Force Microscopy (PiFM) - Principles and Implementations. *Chem. Soc. Rev.* **2022**, *51* (11), 4208−4222.

(55) Latour, R. A. The Langmuir Isotherm: A Commonly Applied but Misleading Approach for the Analysis of Protein Adsorption Behavior. *J. Biomed Mater. Res. A* **2015**, *103* (3), 949−958.

(56) Foo, K. Y.; Hameed, B. H. Insights into the Modeling of Adsorption Isotherm Systems. *Chem. Eng. J.* **2010**, *156* (1), 2−10.

(57) Kastantin, M.; Langdon, B. B.; Schwartz, D. K. A Bottom-up Approach to Understanding Protein Layer Formation at Solid-Liquid Interfaces. *Adv. Colloid Interfac* **2014**, *207*, 240−252.

(58) Kalam, S.; Abu-Khamsin, S. A.; Kamal, M. S.; Patil, S. Surfactant Adsorption Isotherms: A Review. *Acs Omega* **2021**, *6* (48), 32342−32348.

(59) Rabe, M.; Verdes, D.; Seeger, S. Surface-Induced Spreading Phenomenon of Protein Clusters. *Soft Matter* **2009**, *5* (5), 1039−1047.

(60) Hook, F.; Rodahl, M.; Kasemo, B.; Brzezinski, P. Structural Changes in Hemoglobin during Adsorption to Solid Surfaces: Effects of PH, Ionic Strength, and Ligand Binding. *Proc. National Acad. Sci.* **1998**, *95* (21), 12271−12276.

(61) Hoffman, A. S. Non-Fouling Surface Technologies. *J. Biomaterials Sci. Polym. Ed* **1999**, *10* (10), 1011−1014.

https://doi.org/10.1021/acsami.4c07528